




Observation of enhanced sensing response and recovery time of lutetium-doped zinc ferrite ceramics for humidity sensor application

Sofia Sultana Laxmeshwar¹, Soumya S. Kulkarni¹, Shainaz Nadaf¹, K. M Swathi¹, Hemantkumar M. Savanur¹, B Chethan², V. Prasad², V Jagadeesha Angadi^{3,*} , Mohd Ubaidullah⁴, Bidhan Pandit⁵, and Lavish Kansal⁶

¹ Department of P. G. Studies in Chemistry, P. C. Jabin Science College, Hubballi 31, India

² Department of Physics, Indian Institute of Science, Bengaluru 12, India

³ Department of Physics, P. C. Jabin Science College, Hubballi 31, India

⁴ Department of Chemistry, College of Science, King Saud University, P.O. Box 2455, Riyadh 11451, Saudi Arabia

⁵ Department of Materials Science and Engineering and Chemical Engineering, Universidad Carlos III de Madrid, Avenida de la Universidad 30, 28911 Leganés, Madrid, Spain

⁶ School of Electronics and Electrical Engineering, Lovely Professional University, Phagwara, India

Received: 8 August 2023

Accepted: 14 October 2023

Published online:
27 October 2023

© The Author(s), under exclusive licence to Springer Science+Business Media, LLC, part of Springer Nature, 2023

ABSTRACT

It is crucial to have an effective and efficient humidity sensing material for humidity sensor applications. In this study, Lu³⁺-doped Zinc ferrites were prepared by chemical synthesis method using urea and glucose as fuels for the first time. The prepared powder samples were subjected to several analyses, including X-ray diffraction (XRD), Fourier transform infrared spectroscopy (FTIR), Scanning electron microscopy (SEM), and Energy-dispersive X-ray spectroscopy (EDX), to examine the structural and morphological changes in ZnFe_{2-x}Lu_xO₄ (where x = 0, 0.1, 0.3, 0.5, and 0.7). The XRD results show that a single phase was formed without any impurity peak, as confirmed by XRD. The FTIR spectra exhibited two prominent bands at 532 cm⁻¹ and 360 cm⁻¹, which are characteristic features of spinel ferrite. SEM micrographs revealed that the nanoparticles were almost spherical in shape, porous in nature, and fairly uniform in size. Further analysis of the nanoparticle with EDAX confirmed the elemental composition. The humidity sensing behavior of Lu-doped ZnFe₂O₄ was tested in the relative humidity range of 11 to 97%. Among the samples, Lu = 0.05 exhibited the highest sensing response of 97% with response and recovery times of 35.6 and 6.5 s, respectively. Hence, our results suggest that the synthesized samples are useful for humidity sensor applications.

Address correspondence to E-mail: jagadeeshbub@gmail.com

E-mail Addresses: mtayyab@ksu.edu.sa

<https://doi.org/10.1007/s10854-023-11480-w>

1 Introduction

Ferrites are attracted due to their outstanding dielectric and magnetic properties in energy storage and high-frequency application [1]. Metal oxides having spinel structures are known as spinel ferrite materials. They have the general chemical formula AB_2O_4 , where A and B represent various metal cations that are located in the tetrahedral (A-site) and octahedral (B-site) locations, respectively. The types, quantities, and locations of the metal cations in the crystal structure strongly influence the physical and chemical characteristics of ferrites [2, 3]. Numerous industries use spinel ferrites (MFe_2O_4), including gas sensors [4], electrode materials, microwave technology [5], environmental cleanup, and catalysis [6]. For use as magneto-optical devices, single-phase spinel ferrite nanoparticles must have their magnetic characteristics altered by physical and structural factors, such as cation distribution, grain size, and shape [7–9]. Fe_3O_4 , Co_3O_4 , Al_3O_3 , $CoFe_2O_4$, $CuFe_2O_4$, $MnFe_2O_4$, $NiFe_2O_4$, and $ZnFe_2O_4$ are the most prevalent spinel ferrites [10].

The electromagnetic properties of ferrites [11–13] are enhanced by rare earth (RE) ions. With minimal concentration, rare earth (RE) metal ion dopants such as Gd^{3+} , La^{3+} , Nd^{3+} , Sm^{3+} , and Dy^{3+} cause significant changes in SF. [14–17]. Due to their 4f electrons in f–f transitions inside or between f–d configurations, rare earth luminous materials have high color purity, stable physical and chemical properties, good resistance to high-power electron beams, restricted emission band spectra, and stable physical and chemical properties [18–20].

The rare earth-doped ferrites are potentially useful for both low- and high-frequency applications, including transformer cores, multilayered chip inductors, information storage systems, ferrofluid applications, magneto-caloric refrigeration, and magnetic diagnostics [27–29]. These ferrites also have high resistivity, high saturation magnetization, low loss, and high initial permeability. Ferrimagnetic properties can be found in the zinc ferrite, which has an inverted spinel structure. Tetrahedral sites (A-site) are occupied by trivalent Fe^{3+} ions, while octahedral sites (B-site) are occupied by divalent Zn^{2+} ions [30, 31].

The development of the smallest, least expensive humidity sensors, as well as improving repeatability, reproducibility, timing behavior, high sensing responsiveness, a lower limit of detection, and room-temperature operability, present challenges to researchers.

Due to their advantageous characteristics, such as high sensitivity, simple production, room-temperature operability, water absorption, compactness, and exceptional performance, conducting nanocomposite-based sensors are frequently utilized to address these problems [32]. The mechanical and electrical characteristics of these nanocomposites can be altered by doping and constructing composites using a variety of synthetic techniques [33]. Numerous researchers' interest in Zn–Fe nanoparticles has recently increased as a result of their intriguing applications, which include low corrosion, low cost, ease of preparation, lack of need for complicated tools, excellent workability, strong environmental stability, and distinctive transport features [34]. Sensors and electronic devices are just two examples of the many applications for Zn–Fe nanoparticles [35]. Despite having all the aforementioned benefits, Zn–Fe nanoparticles still perform poorly at higher relative humidity levels, and it is necessary to improve their timing behavior [21–26, 36].

Further there is no report on rare earth Lu-doped ferrites for humidity sensors. In the present work, we have synthesized $ZnFe_{(2-x)}Lu_xO_4$ ($X=0, 0.01, 0.03, 0.05$, and 0.07) by chemical synthesis method to study the structural, microstructural, infrared and humidity sensing properties.

2 Experimental method

2.1 Synthesis of $ZnFe_{(2-x)}Lu_xO_4$

Nanoparticles of $ZnFe_{(2-x)}Lu_xO_4$ (where $X=0.00, 0.01, 0.03, 0.05, 0.07$)(ZFL) were synthesized by chemical synthesis method. To prepare them, stoichiometric molar amounts of zinc nitrate ($Zn(NO_3)_2 \cdot 6H_2O$), iron nitrate ($Fe(NO_3)_2 \cdot 6H_2O$), and lutetium nitrate ($Lu(NO_3)_2 \cdot 9H_2O$) were taken in a 250-mL beaker, which acted as oxidizers. Glucose and urea in 1:1 ratio were added to this along with 15 mL of distilled water and the resultant mixture was stirred to obtain a homogeneous solution containing a redox mixture.

The beaker contains all the solution of metal nitrates and fuels and were placed in a preheated muffle furnace ($450\text{ }^\circ\text{C}$) for approximately 30 min. Initially, the solution is boiled and ignited to form a gel, which is then burned into powder, releasing stable gases, like CO_2 , N_2 , and H_2O . The redox reactions taking place can be represented in the form of the proposed Eq. 1 as given below:

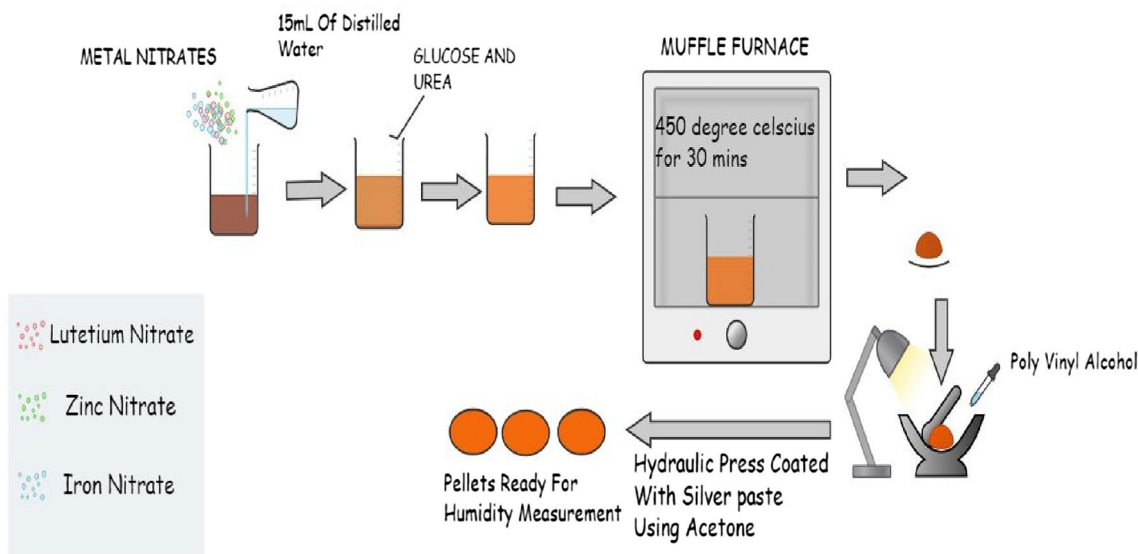
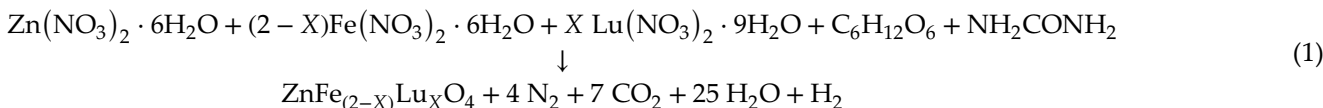


Fig. 1 Graphical representation for the preparation of nanoparticles

Table 1 Stoichiometric amount of oxidizers and fuels used in the synthesis method

Lutetium nitrate in M	Zinc nitrate in g	Lutetium nitrate in g	Iron nitrate in g	Urea in g	Glucose in g
0.00	1.841	0	5	1.239	0.929
0.01	1.850	0.0225	5	1.245	0.934
0.03	1.869	0.0680	5	1.258	0.943
0.05	1.888	0.1146	5	1.271	0.953
0.07	1.908	0.1620	5	1.284	0.963



The stoichiometric calculations are shown in Table No 1. The graphical representation of synthesis method is shown in Fig. 1.

3 Results and discussion

3.1 Structure analysis by XRD

The XRD patterns of $\text{ZnFe}_{(2-x)}\text{Lu}_x\text{O}_4$ (where $X = 0.00, 0.01, 0.03, 0.05, 0.07$) is represented in Fig. 2. The XRD patterns were recorded in the 2θ ranging from 20° to 80° at suitable temperature. The presence of the cubic characteristic peaks (220), (311), (222), (400), (422),

(511), and (440) at $29.9^\circ, 35.2^\circ, 42.6^\circ, 53.2^\circ, 56.7^\circ,$ and 62.26° in XRD diffraction patterns of all samples indicates that the prepared samples are pure and not contains any kind of impurity. These peaks confirmed the good crystallinity as well as cubic spinel structure.

The average crystallite size was calculated using Eq. 2. The size of the prepared nanoparticles is found in the range from 28 to 22 nm. The crystallite size will decrease with increasing Lu^{3+} concentration. Studies have shown that incorporating rare earth ions with sizable radii, like Lutetium(3+) into Zinc ferrites in place of ferric ions, results in significant strain and decreases crystallite size.

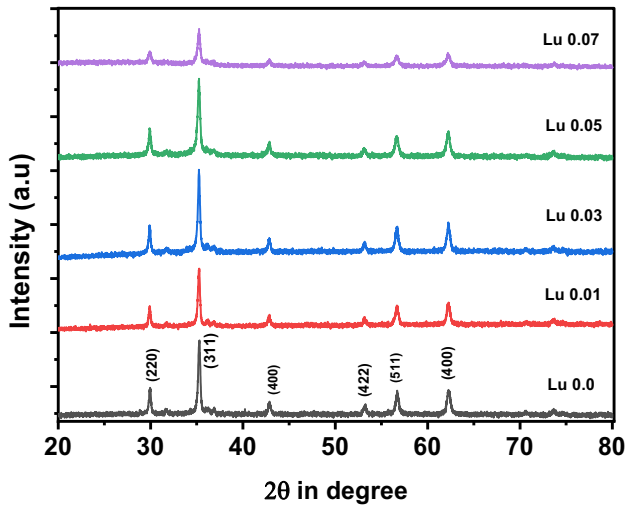


Fig. 2 XRD patterns of $ZnFe_{(2-x)}Lu_xO_4$ (where $X=0.00, 0.01, 0.03, 0.05, 0.07$)

$$D = \frac{(K.\lambda)}{(\beta. \cos \theta)} \tag{2}$$

where D is the crystallite size (nm), K is the Scherrer constant (0.89), λ is the wavelength, β is the full width at half maximum in radians, and θ is the Bragg's angle.

Because of the lattice distortion induced by the difference in radius between the dopant and the element being replaced, the crystalline size may also decrease as the ion concentration increases. The crystallite size v/s Lu concentration is shown in Fig. 3.

Further Lattice constant (a) is calculated using Eq. 3.

$$a = \frac{\lambda \sqrt{h^2 + l^2 + k^2}}{2\text{Sin}\theta} \tag{3}$$

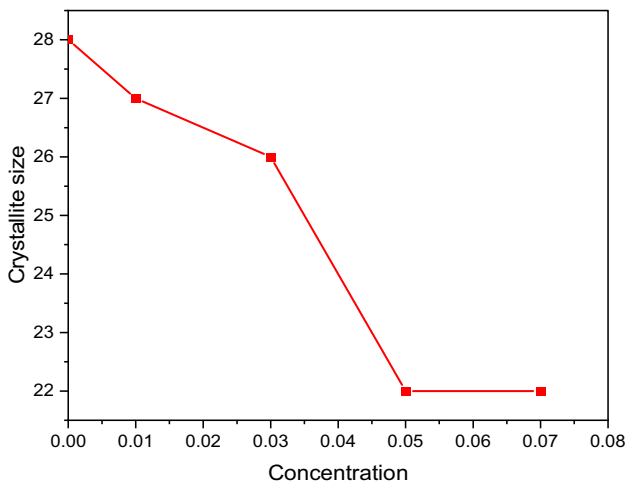


Fig. 3 Crystallite size v/s Concentration

where $\frac{\lambda}{2 \sin \theta} = d_{hkl}$ (interlunar spacing) and h,k,l , are miller indices.

The lattice parameter were found to decrease with increasing with rare earth concentration and crystal-lite size. The lattice parameter of Zn ferrite is reduced when Lu^{3+} is substituted, due to micro-strain in the internal grain region. This micro-strain is caused by compression resulting from differences in the thermal expansion coefficient between constituent elements or lattice mismatches between the grain and the grain boundary phase.

Unit cell volume (V) is calculated using Eq. 4 as below:

$$V = a^3 \tag{4}$$

The distance between the magnetic ions at tetra-hedral (A) and octahedral (B) sites was calculated using the following Eqs. 5 and 6.

$$L_a = \frac{a\sqrt{3}}{4} \tag{5}$$

$$L_b = \frac{a\sqrt{3}}{2} \tag{6}$$

As the concentration of the nanoparticles increases, more and more particles begin to interact with each other, causing the volume to increase as the particles begin to aggregate or form clusters. However, at very high concentrations, the particles become crowded that there is no enough space for additional particles to contribute to volume, so the volume decreases and the usual trend is seen and all values are presented in Table 2.

Table 2 Parameter of $Zn Fe_{2-x}Lu_xO_4$

X	Crystallite site (D) nm	Lattice parameter	Volume A^3	L_A	L_B
0	28	8.441	602	3.654	2.297
0.01	27	8.446	603	3.657	2.981
0.03	26	8.444	602	3.656	2.981
0.05	22	8.517	605	3.656	2.980
0.07	22	8.446	603	3.623	2.980

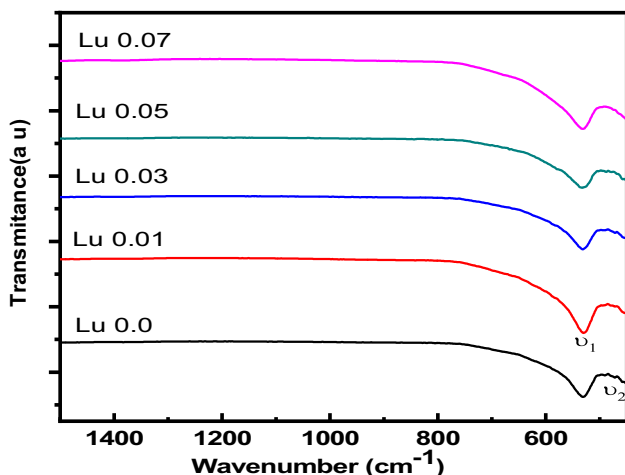


Fig. 4 FTIR spectra of Lu-doped Zn ferrite, i.e., Lu 0.00 = ZnFe_2O_4 , Lu 0.01 = $\text{ZnFe}_{1.99}\text{Lu}_{0.01}\text{O}_4$, Lu 0.03 = $\text{ZnFe}_{1.97}\text{Lu}_{0.03}\text{O}_4$, Lu 0.05 = $\text{ZnFe}_{1.95}\text{Lu}_{0.05}\text{O}_4$, and Lu 0.07 = $\text{ZnFe}_{1.93}\text{Lu}_{0.07}\text{O}_4$

3.2 Fourier transform infrared spectroscopy (FTIR) studies

In Fig. 4, we can see the FTIR spectrum for $\text{ZnFe}_{(2-x)}\text{Lu}_x\text{O}_4$ (where $X = 0.00, 0.01, 0.03, 0.05, 0.07$). The spectrum shows two absorption bands at 532 cm^{-1} (ν_1) and 480 cm^{-1} (ν_2), which correspond to the tetrahedral and octahedral complexes, respectively. The difference between the ν_1 and ν_2 modes is due to changes in the bond length (Fe–O) at the A-sites (tetrahedral) and B-sites (octahedral). The preparation process, grain size, and porosity also affect the band location of ν_1 and ν_2 . The absence of splitting or shouldering in the absorption band ν_1 rules out the potential of Fe^{2+} ions at A-sites. On the other hand, the splitting or shoulders observed in absorption band ν_2 are due to the Jahn–Teller distortion caused by Fe^{2+} ions on B-sites, which cause lattice deformation due to a non-cubic component of the crystal field potential. The presence of Lu^{3+} at the octahedral site is confirmed by the shift of the absorption band ν_2 toward the low frequency. Furthermore, as Lu^{3+} replaces Fe^{3+} ions at B-sites, fewer Fe^{3+} ions are present, resulting in the shift of the band at 1 to a higher wave number area. The introduction of Lu^{3+} ions into the Fe^{3+} and O_2 - link at each octahedral and tetrahedral site causes changes in the absorption bands ν_1 and ν_2 , leading to structural distortion in Zn ferrites.

3.3 SEM with EDS analysis

To get microstructural photos, such as grain size, pores, inclusions, grain borders, particle size, homogeneity, and fluxes, SEM is utilized. Other microstructural features that can be viewed include grain boundaries. Because of the smaller grain size and lower porosity, the production of undesired spin waves is reduced, which is something that is necessary for humidity sensors. The sample's high porosity contributes to an improvement in the way it senses humidity in the environment.

The EDS spectra were used to conduct an elemental analysis on the samples that had been manufactured. It can be seen from the EDS spectra of all of the samples, which can be found in Fig. 5b that the compositions that were intended to be synthesized did so according to the chemical equations. The theoretical stoichiometry and the experimental stoichiometry that was estimated from the EDS data agree quite well with one another. This demonstrates that the particles have distinct grain boundaries as a result of their growth. It can be seen quite plainly that the particles are virtually perfectly spherical, and there is considerable aggregation combined throughout the preparation process,

apparent in all of the compositions. The presence of Fe borders can be quantitatively described using the EDS patterns. It can be seen quite plainly that the particles are virtually perfectly spherical, and there is considerable aggregation apparent in all of the compositions. The EDS patterns provide a quantitative description of the presence of many elements in ferrite materials, including Fe, Zn, Lu, and O. The EDS analysis delivered an accurate calculation of the elements concentrations in accordance with the specifications that were provided.

3.4 Humidity sensing behavior

3.4.1 Humidity sensing set-up

Humidity sensing analysis was conducted using glass chambers filled with salt solutions and supervised by a humidity meter (Mextech-DT-615). Rubber cork electrodes sealed the compartments. The sample in the form of pellets were connected to electrodes with the help of programmable digital multimeter, Hioki DT 4282, to obtain resistance measurements upon being exposed to a specific relative humidity environment

Series	Element	Mass %
Lu (0.00) (a) Lu 0.0	C	22 (a)
	O	31.86
	Fe	45.86
	Total	100.00
Lu (0.01) (b) Lu 0.01	O	23.20
	Fe	47.9 (b)
	Zn	28.86
	Total	100.00
Lu (0.03) (c) Lu 0.03	C	20.24
	O	29.83
	Fe	28 (c)
	Zn	20.17
	Lu	0.89
	Total	100.00
Lu (0.05)	C	17.29
	O	32.37
	Na	1.07
	Fe	28.91
	Zn	18.96
	Lu	1.39
	Total	100.00
Lu (0.07)	C	38.68
	O	30.68
	Na	0.68
	Fe	17.42

Fig. 5 a and b: The SEM micrographs and EDS spectra of Lu-doped Zn ferrite. **a** Lu 0.00 = ZnFe_2O_4 , **b** Lu 0.01 = $\text{ZnFe}_{1.99}\text{Lu}_{0.01}\text{O}_4$, **c** Lu 0.03 = $\text{ZnFe}_{1.97}\text{Lu}_{0.03}\text{O}_4$, **d** Lu 0.05 = $\text{ZnFe}_{1.95}\text{Lu}_{0.05}\text{O}_4$, and **e** Lu 0.07 = $\text{ZnFe}_{1.93}\text{Lu}_{0.07}\text{O}_4$

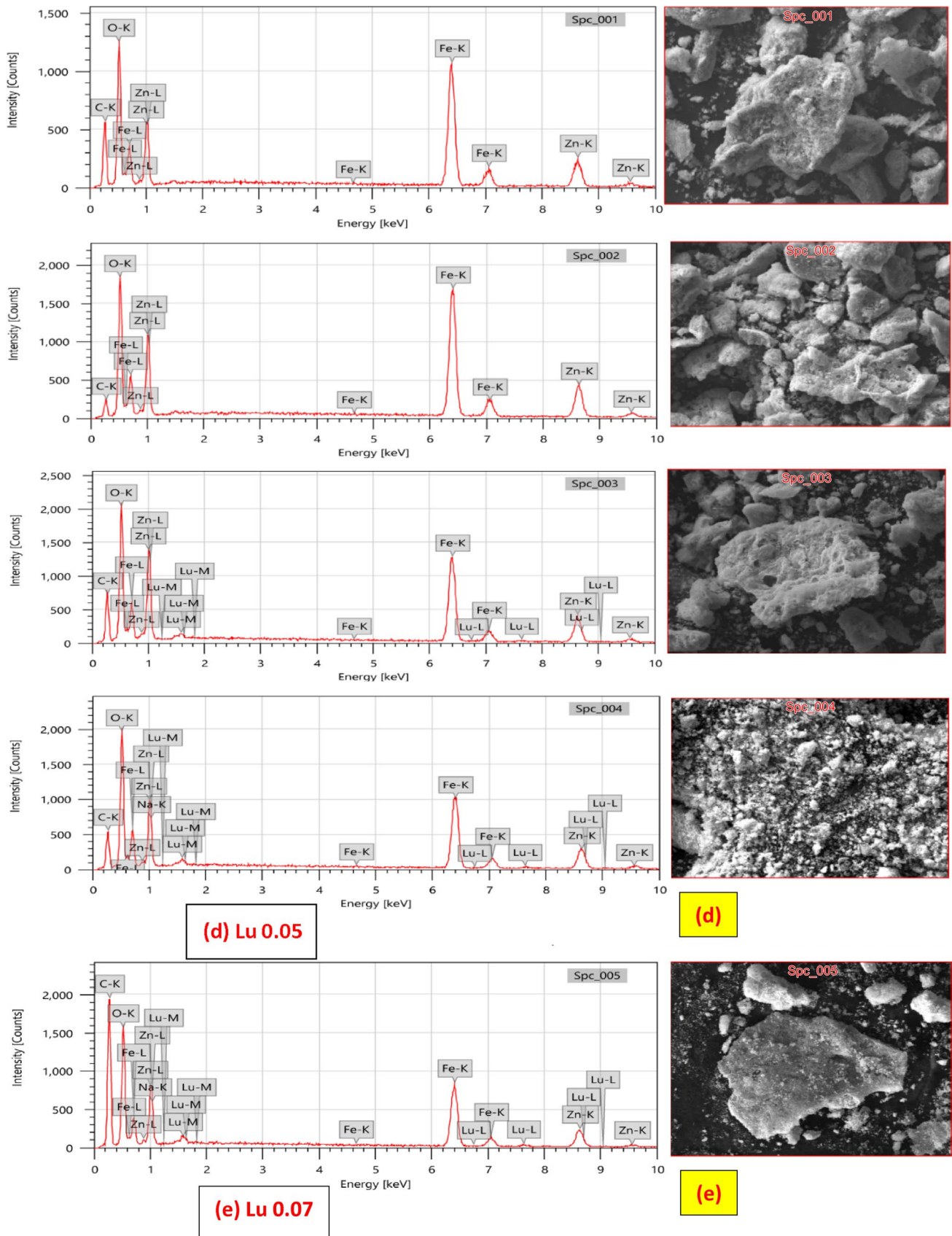


Fig. 5 continued

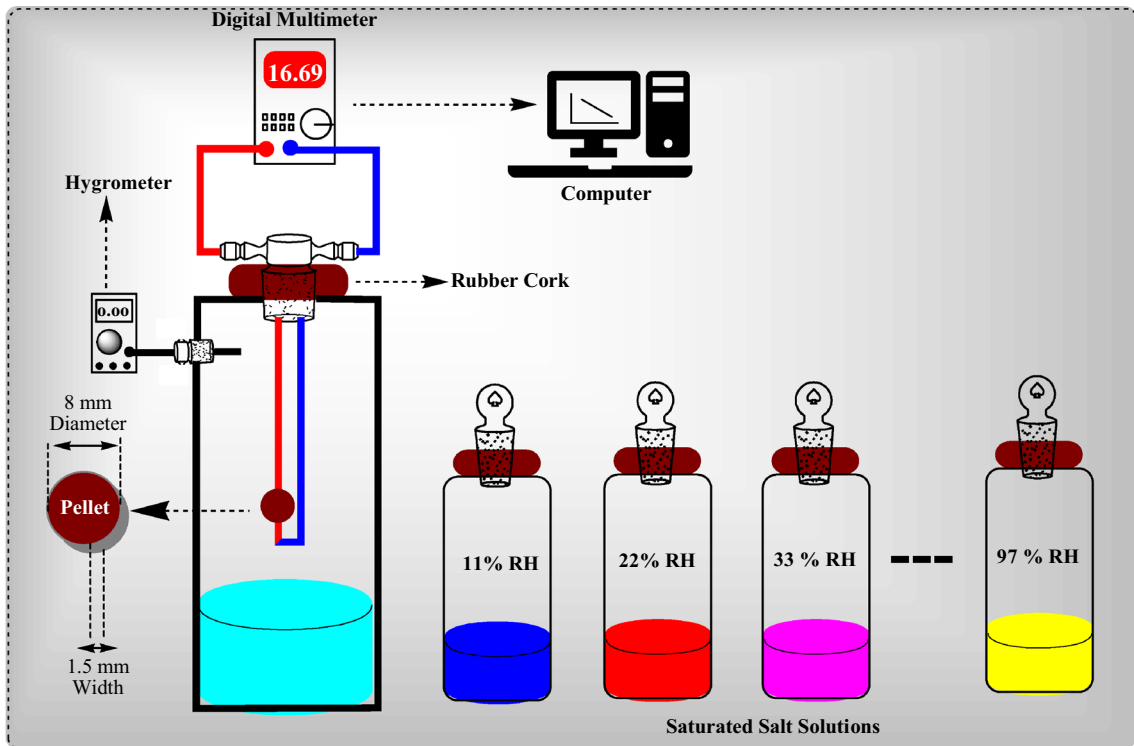


Fig. 6 Humidity sensing study set-up

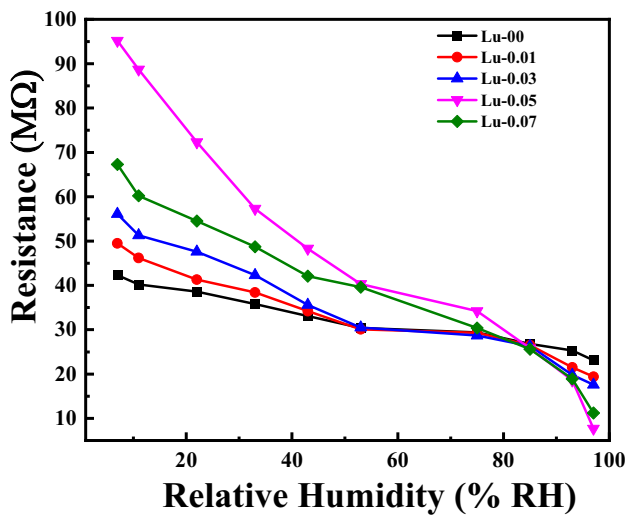


Fig. 7 The change in resistance versus % RH

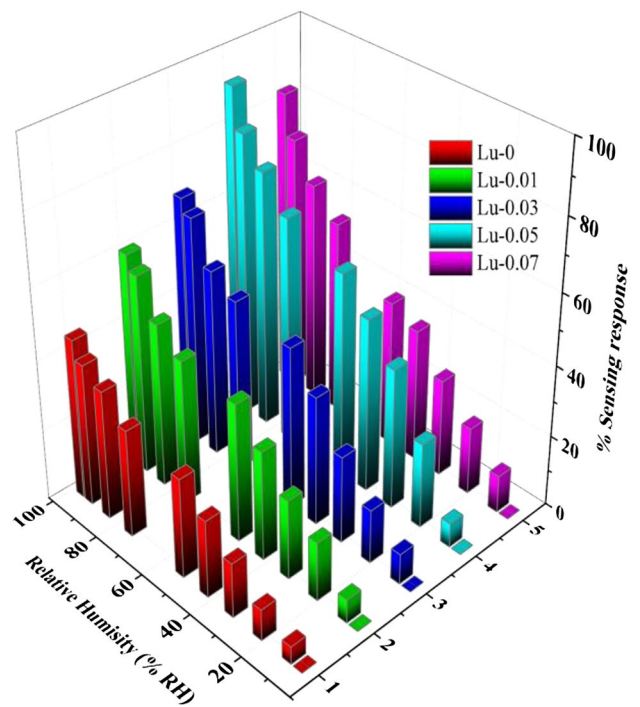


Fig. 8 The sensing response of ZnFe_(2-x)Lu_xO₄ (where X= 0.00,0.01,0.03,0.05,0.07)

at room temperature. Figure 6 illustrates the humidity sensor set-up for humidity sensing experiments.

3.4.2 Humidity sensing studies

Figure 7 illustrates the resistance v/s relative humidity of Lu-doped Zn ferrite samples with varying Lu compositions. Among all the samples, $\text{ZnFe}_{1.95}\text{Lu}_{0.05}\text{O}_4$ exhibits the most significant resistance shift and achieved a sensing performance of almost 97%. This is attributed to the more porous and active surface of the nanoparticles, which absorb water vapor and provide a site for proton seeking, resulting in a decrease in resistivity. Figure 8 compares the variation in sensing response.

3.4.3 Timing behavior

The most crucial component for comprehending the sensor's capabilities is timing. The time parameter was calculated using two flasks, one kept at 11% relative humidity and the other at 97% RH. Next, the relative humidity (RH) of each film was quickly changed from 11 to 97%, and the matching response

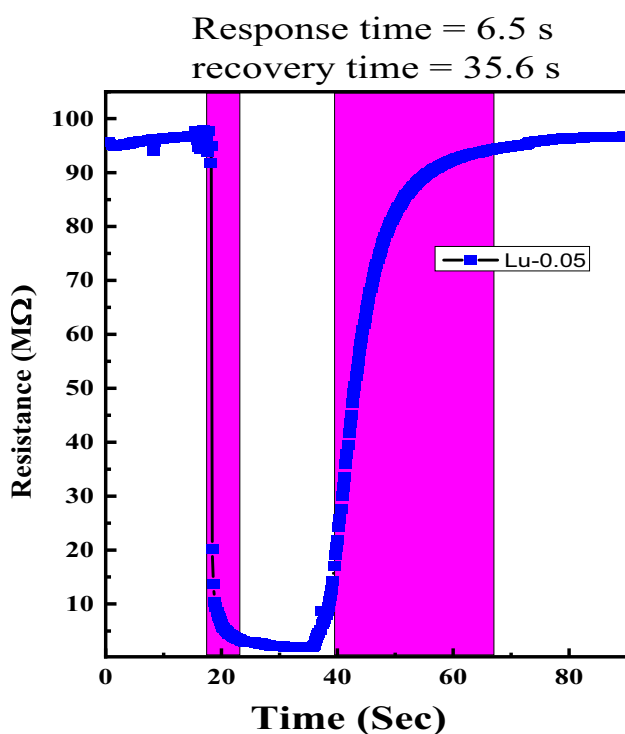


Fig. 9 The timing behavior of the $\text{ZnFe}_{1.95}\text{Lu}_{0.05}\text{O}_4$ nanoparticles

and recovery times were recorded. The changing time in each situation was 35.6 s [37]. The proper plots for reaction and recovery behaviors are shown in Fig. 9. Additionally, it is clear that the Lu 0.05 composite has a 35.6-s recovery time and a 6.5-s response time. This time, behavior was established because the composite has a high-porosity surface and a larger surface area. Due to the spontaneous nature of adsorption, which needs greater energy to break the link between the adsorbent and adsorbed surface, response, and recovery times differ [38–46]. The outstanding quality is that the short reaction and recovery time of the Lu 0.05 composite have produced a good sensing response.

3.4.4 Hysteresis

In the region of 11% RH to 97% RH, the experimental humidity hysteresis characteristic for the 5 mol%-substituted $\text{ZnFe}_{2-x}\text{Lu}_x\text{O}_4$ nanoparticles was identified, as shown in Fig. 10. The absorption curve was obtained by retracing the means in equivalent measure, and the desorption curve is shown by a progressive increase from 11% RH to 97% RH.

The process of absorption has been observed to be a little slower than the process of desorption. This means that exothermic and endothermic responses, when compared individually to adsorption and desorption, occur at different rates, resulting in impedance becoming slightly higher and lower when absorbing than when desorbing. The most extreme wetness hysteresis,

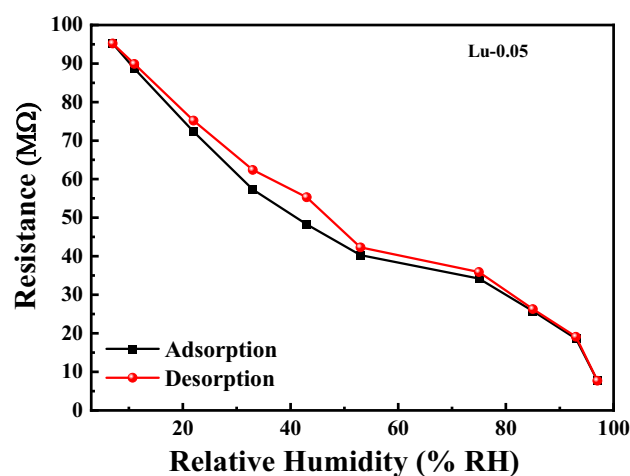


Fig. 10 The humidity hysteresis of the $\text{ZnFe}_{1.95}\text{Lu}_{0.05}\text{O}_4$ nanoparticles

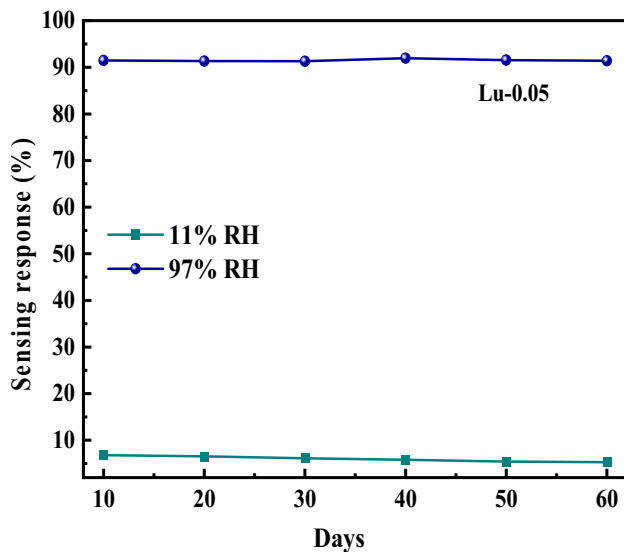


Fig. 11 The humidity stability of the ZnFe_{1.95}Lu_{0.05}O₄ nanoparticles

which is also visible in the image, is around 3% at 55% relative humidity, and the results are well matched to the praseodymium-doped magnesium ferrite [46].

3.4.5 Humidity stability

For a period of two months, the stability of the ZnFe_{1.95}Lu_{0.05}O₄ nanoparticles was assessed every 10 days. For 11% and 97%, the sensing response was determined every 10 days and a graph showing the relationship between the two was drawn. Figure 11 displays the charts for humidity sensing. This ZnFe_{1.95}Lu_{0.05}O₄ nanoparticles sensor is more effective and suitable for industrial applications due to its epitome sensitivity, maximum change in resistance, good response and recovery, minimal hysteresis, and maximum stability.

4 Conclusion

Ultimately, the nanomaterial ZnFe_{2-x}Lu_xO₄, synthesized by the solution combustion method to minimize time consumption, has successfully shown a very effective sensing response at room temperature. Further, the compound prepared when subjected to XRD analysis discloses a crystal size in the range of

28–22 nm due to the increase in lutetium concentration. Sequentially, the SEM micrographs show the porosity of nanoparticles with different morphological features. The analysis of FTIR bands at 532 cm⁻¹ and 480 cm⁻¹ confirms the formation of Fe nanoparticle. A remarkable sensing response of 97% was observed in the range of 11–97% RH with the feature of increasing resistivity with the increase in the concentration of lutetium, and the material has shown a recovery time of 35.6 s and a response time of 6.5 s. Consequently, with the evaluation of no hysteresis it is concluded that the material is found to be exceptionally stable. In conclusion, the synthesized ferrites nanomaterial can be advantageous for the low cost, efficient, and less time consuming with ease of preparation for the humidity sensing devices at room temperature. Overall, the nanomaterial can be considered for the large-scale industrial applications.

Acknowledgements

The authors extend their sincere appreciation to the Researchers Supporting Project number (RSPD2023R682), King Saud University, Riyadh, Saudi Arabia for the support.

Author contributions

SSL contributed to the conceptualization, methodology, software, and writing and original draft preparation, SSK contributed to analysis and original draft preparation. SN contributed to reviewing of the manuscript and original draft preparation. SKM contributed to analysis and original draft preparation. HMS contributed to analysis and editing of the manuscript. CB contributed to Humidity analysis. VP contributed to Editing of the manuscript. JAV contributed to editing of the manuscript. MU contributed to editing of the manuscript. BP contributed to analysis of humidity data. LK contributed to editing of the manuscript.

Funding

This study was supported by Researchers Supporting Project number (RSPD2023R682), King Saud University, Riyadh Saudi Arabia.

Data availability

The datasets generated during and/or analyzed during the current study are available from the corresponding author on reasonable request. The data that support the findings of this study are not openly available due to unpublished work anywhere and are available from the corresponding author upon reasonable request

Declarations

Conflict of interest The authors declare that they have no known competing financial interests or personal relationships that could have appeared to influence the work reported in this paper.

References

1. S. Liu, W. Feng, J. Li, C. Zhao, C.H.B. He, Z. Bao, X. Luan, Achieving high energy storage density and efficiency simultaneously in Sr (Nb_{0.5}Al_{0.5})O₃ modified BiFeO₃ based lead-free ceramics. *Chem. Eng. J.* **451**, 138916 (2023). <https://doi.org/10.1016/j.cej.2022.138916>
2. Reddy, D.H. Kumar, Y.-S. Yun, Spinel ferrite magnetic adsorbents: alternative future materials for water purification? *Coord. Chem. Rev.* **315**, 90–111 (2016). <https://doi.org/10.1016/j.ccr.2016.01.012>
3. K.K. Kefeni, B.M. Bhekie, Photocatalytic application of spinel ferrite nanoparticles and nanocomposites in wastewater treatment. *Sustain. Mater. Technol.* **23**, e00140 (2020). <https://doi.org/10.1016/j.susmat.2019.e00140>
4. H. Qin, Y. He, P. Xu, D. Huang, Z. Wang, H. Wang, Z. Wang, Y. Zhao, Q. Tian, C. Wang, Spinel ferrites (MFe₂O₄): synthesis, improvement and catalytic application in environment and energy field. *Adv. Colloid Interface Sci.* **294**, 102486 (2021). <https://doi.org/10.1016/j.cis.2021.102486>
5. J. Ma, B. Zhao, H. Xiang, F.-Z. Dai, Y. Liu, R. Zhang, Y. Zhou, High-entropy spinel ferrites MFe₂O₄ (M = mg, Mn, Fe, Co, Ni, Cu, Zn) with tunable electromagnetic properties and strong microwave absorption. *J. Adv. Ceram.* **11**(5), 754–768 (2022). <https://doi.org/10.1007/s40145-022-0569-3>
6. Y. Ding, L. Zhu, N. Wang, H. Tang, Sulfate radicals induced degradation of tetrabromobisphenol A with nanoscaled magnetic CuFe₂O₄ as a heterogeneous catalyst of peroxy monosulfate. *Appl. Catal. B* **129**, 153–162 (2013). <https://doi.org/10.1016/j.apcatb.2012.09.015>
7. D. Ravinder, M. Hashim, A. Upadhyay, M.M. Ismail, S. Kumar, R. Kumar, S.S. Meena, Ahmad Khalilullah, Investigation of structural and magnetic properties of La doped Co–Mn ferrite nanoparticles in the presence of α-Fe₂O₃ phase. *Solid State Commun.* **342**, 114629 (2022). <https://doi.org/10.1016/j.ssc.2021.114629>
8. R.S. Priya, P. Chaudhary, E. Ranjith Kumar, A. Balamurugan, Ch. Srinivas, G. Prasad, M. Deepty et al., Effect of heat treatment on structural, morphological, dielectric and magnetic properties of Mg–Zn ferrite nanoparticles. *Ceram. Int.* **48**(11), 15243–15251 (2022). <https://doi.org/10.1016/j.ceramint.2022.02.056>
9. H. Mahajan, S.K. Godara, A.K. Srivastava, Synthesis and investigation of structural, morphological, and magnetic properties of the manganese doped cobalt-zinc spinel ferrite. *J. Alloys Compd.* **896**, 162966 (2022). <https://doi.org/10.1016/j.jallcom.2021.162966>
10. F. Valente, L. Astolfi, E. Simoni, S. Danti, V. Franceschini, Milvia Chicca, and Alessandro Martini. Nanoparticle drug delivery systems for inner ear therapy: an overview. *J. Drug Deliv. Sci. Technol.* **39**, 28–35 (2017). <https://doi.org/10.1016/J.JDDST.2017.03.003>
11. S.E. Jacobo, S. Duhalde, H.R. Bertorello, Rare earth influence on the structural and magnetic properties of NiZn ferrites. *J. Magn. Magn. Mater.* **272**, 2253–2254 (2004). <https://doi.org/10.1016/j.jmmm.2003.12.564>
12. R.H. Kadam, R.B. Borade, M.L. Mane, D.R. Mane, K.M. Batoo, S.E. Sagar, Structural, mechanical, dielectric properties and magnetic interactions in Dy³⁺-substituted Co–Cu–Zn nanoferrites. *RSC adv.* **10**(47), 27911–27922 (2020). <https://doi.org/10.1039/D0RA05274D>
13. M. Baig, S. Mahmood, M.A. Zulfiquar, M. Yousuf, S. Touqeer, P.O. Ullah, M.F. Agboola, Warsi, I. Shakir, Structural and photocatalytic properties of new rare earth La³⁺ substituted MnFe₂O₄ ferrite nanoparticles. *Ceram. Int.* **46**(14), 23208–23217 (2020). <https://doi.org/10.1021/acsaem.9b00317>
14. Y. Slimani, M.A. Almessiere, A. Demir Korkmaz, S. Guner, H. Güngüneş, M. Sertkol, A. Manikandan et al., Ni_{0.4}Cu_{0.2}Zn_{0.4}Tb_xFe_{2-x}O₄ nanospinel ferrites: ultrasonic synthesis and physical properties. *Ultrason. Sonochem.* **59**, 104757 (2019)
15. M.A. Almessiere, Y. Slimani, A.D. Korkmaz, A. Baykal, H. Güngüneş, H. Sözeri, S.E. Shirsath, S. Güner, S. Akhtar, A. Manikandan, Impact of La³⁺ and Y³⁺ ion substitutions on structural, magnetic and microwave properties of Ni_{0.3}Cu_{0.3}Zn_{0.4}Fe₂O₄ nanospinel ferrites synthesized via

- sonochemical route. RSC Adv. **9**(53), 30671–30684 (2019). <https://doi.org/10.1016/j.ultsonch.2019.104847>
16. M. Almessiere, Y. Abdullah, S. Slimani, M. Guner, A. Sertkol, S.E. Demir Korkmaz, Shirsath, A. Baykal, Sonochemical synthesis and physical properties of $\text{Co}_{0.3}\text{Ni}_{0.5}\text{Mn}_{0.2}\text{Eu}_x\text{Fe}_{2-x}\text{O}_4$ nano-spinel ferrites. Ultrason. Sonochem. **58**, 104654 (2019). <https://doi.org/10.1016/j.ultsonch.2019.104654>
 17. Y. Slimani, M. Munirah Abdullah Almessiere, S.E. Sertkol, A. Shirsath, M. Baykal, S. Nawaz, B.E.K.Ä.R. Akhtar, Ozcelik, I. Ercan, Structural, magnetic, optical properties and cation distribution of nanosized $\text{Ni}_{0.3}\text{Cu}_{0.3}\text{Zn}_{0.4}\text{TM}_x\text{Fe}_{2-x}\text{O}_4$ ($0.0 \leq x \leq 0.10$) spinel ferrites synthesized by ultrasound irradiation. Ultrason. Sonochem. **57**, 203–211 (2019). <https://doi.org/10.1016/j.ultsonch.2019.05.001>
 18. S. Gai, C. Li, P. Yang, J. Lin, Recent progress in rare earth micro/nanocrystals: soft chemical synthesis, luminescent properties, and biomedical applications. Chem. Rev. **114**(4), 2343–2389 (2014). <https://doi.org/10.1021/cr4001594>
 19. J. Zhou, Q. Liu, W. Feng, Y. Sun, F. Li, Upconversion luminescent materials: advances and applications. Chem. Rev. **115**(1), 395–465 (2015). <https://doi.org/10.1021/cr400478f>
 20. A.M. Liu, Jing, Kaczmarek, and Rik Van Deun Advances in tailoring luminescent rare-earth mixed inorganic materials. Chem. Soc. Rev. **47**(19), 7225–7238 (2018). <https://doi.org/10.1039/C7CS00893G>
 21. A.M. Pachpinde, M.M. Langade, K.S. Lohar, S.M. Patange, E. Sagar, Shirsath. Impact of larger rare earth Pr^{3+} ions on the physical properties of chemically derived $\text{Pr}_x\text{CoFe}_{2-x}\text{O}_4$ nanoparticles. Chem. Phys. **429**, 20–26 (2014). <https://doi.org/10.1016/j.chemphys.2013.11.018>
 22. G.K. Samudrala, Y.K. Vohra, Structural properties of lanthanides at ultra high pressure, in *Handbook on the physics and chemistry of rare earths*. (Elsevier, Amsterdam, 2013), pp.275–319
 23. K.M. Srinivasamurthy, A. El-Denglawey, K. Manjunatha, M.C. Oliveira, E. Longo, S.R. Lázaro, P. Ribeiro. Observation of dielectric dispersion and relaxation behavior in Ni^{2+} -substituted cobalt ferrite nanoparticles. J. Mater. Chem. C **10**(9), 3418–3428 (2022). <https://doi.org/10.1039/D1TC05980G>
 24. K. Manjunatha, I.C. Sathish, S.P. Kubrin, A.T. Kozakov, T.A. Lastovina, A.V. Nikolskii, K.M. Srinivasamurthy, M. Pasha, Jagadeesha Angadi. X-ray photoelectron spectroscopy and low temperature Mössbauer study of Ce^{3+} substituted MnFe_2O_4 . J. Mater. Sci. **30**, 10162–10171 (2019). <https://doi.org/10.5772/intechopen.99264>
 25. H.R. Lakshmi prasanna, K. Manjunatha, Effect of cerium on structural, microstructural, magnetic and humidity sensing properties of Mn–Bi ferrites. Nano-Structures & Nano-Objects. **24**, 100608 (2020). <https://doi.org/10.1007/s10854-021-05592-4>
 26. P.P. Naik, R.B. Tangsali, S.S. Meena, S.M. Yusuf, Influence of rare earth (Nd^{+3}) doping on structural and magnetic properties of nanocrystalline manganese-zinc ferrite. Mater. Chem. Phys. **191**, 215–224 (2017). <https://doi.org/10.1016/j.matchemphys.2017.01.032>
 27. M. Zheng, X.C. Wu, B.S. Zou, Y.J. Wang, Magnetic properties of nanosized MnFe_2O_4 particles. J. Magn. Magn. Mater. **183**, 1–2 (1998). [https://doi.org/10.1016/S0304-8853\(97\)01057-3](https://doi.org/10.1016/S0304-8853(97)01057-3)
 28. A.C.F.M. Costa, E. Tortella, M.R. Morelli, R.H.G.A. Kiminami, Synthesis, microstructure and magnetic properties of Ni–Zn ferrites. J. Magn. Magn. Mater. **256**, 1–3 (2003). [https://doi.org/10.1016/S0304-8853\(02\)00449-3](https://doi.org/10.1016/S0304-8853(02)00449-3)
 29. A. Verma, T.C. Goel, R.G. Mendiratta, M.I. Alam, Dielectric properties of NiZn ferrites prepared by the citrate precursor method. Mater. Sci. Engineering: B **60**(2), 156–162 (1999). [https://doi.org/10.1016/S0921-5107\(99\)00019-7](https://doi.org/10.1016/S0921-5107(99)00019-7)
 30. S. Kanithan, N. Arun Vignesh, K.M. Katubi, Enhanced optical, magnetic, and photocatalytic activity of Mg^{2+} substituted NiFe_2O_4 spinel nanoparticles. J. Mol. Struct. **1265**, 133289 (2022). <https://doi.org/10.1016/j.molstruc.2022.133289>
 31. D.R. Patil, B.K. Chougule, Effect of copper substitution on electrical and magnetic properties of NiFe_2O_4 ferrite. Mater. Chem. Phys. **117**(1), 35–40 (2009). <https://doi.org/10.1016/j.matchemphys.2008.12.034>
 32. B. Chethan, H.G. Raj Prakash, Y.T. Ravikiran, S.C. Vijaya Kumari, S. Manjunatha, S. Thomas, Humidity sensing performance of hybrid nanorods of polyaniline–Yttrium oxide composite prepared by mechanical mixing method. Talanta **215**, 120906 (2020). <https://doi.org/10.1016/j.talanta.2020.120906>
 33. S.-J. Jung, The characterization of a CuO/ZnO heterocontact-type gas sensor having selectivity for CO gas. Sens. Actuators B **37**, 1–2 (1996). [https://doi.org/10.1016/S0925-4005\(96\)01986-7](https://doi.org/10.1016/S0925-4005(96)01986-7)
 34. Z. Ling, C. Leach, R. Freer, NO_2 sensitivity of a heterojunction sensor based on WO_3 and doped SnO_2 . J. Eur. Ceram. Soc. **23**(11), 1881–1891 (2003). [https://doi.org/10.1016/S0955-2219\(02\)00429-6](https://doi.org/10.1016/S0955-2219(02)00429-6)
 35. S.T. Jun, G.H. Choi, CO gas-sensing properties of 3ZnO/CuO contact ceramics. Sens. Actuators B **17**(3), 175–178 (1994). [https://doi.org/10.1016/0925-4005\(93\)00868-Y](https://doi.org/10.1016/0925-4005(93)00868-Y)
 36. E. Traversa, M. Miyayama, H. Yanagida, Gas sensitivity of $\text{ZnO}/\text{La}_2\text{CuO}_4$ heterocontacts. Sens. Actuators B **17**(3),

- 257–261 (1994). [https://doi.org/10.1016/0925-4005\(93\)00877-2](https://doi.org/10.1016/0925-4005(93)00877-2)
37. F. Fang, J. Kennedy, J. Futter, T. Hopf, A. Markwitz, E. Manikandan, G. Henshaw, Size-controlled synthesis and gas sensing application of tungsten oxide nanostructures produced by arc discharge. *Nanotechnology* **22**(33), 335702 (2011). <https://doi.org/10.1088/0957-4484/22/33/335702>
38. M. Biswas, A. Dey, S.K. Sarkar, Polyaniline based field effect transistor for humidity sensor. *Silicon* **14**(14), 8919–8925 (2022). <https://doi.org/10.1007/s12633-021-01594-3>
39. S. Mansingh, A. Rashmi, M. Satyabadi, K.M. Parida, Pyrochlore Ce₂Zr₂O₇ decorated over rGO: a photocatalyst that proves to be efficient towards the reduction of 4-nitrophenol and degradation of ciprofloxacin under visible light. *Phys. Chem. Chem. Phys.* **20**(15), 9872–9885 (2018). <https://doi.org/10.1039/C8CP00621K>
40. S. Nayak, K.M. Parida, Deciphering Z-scheme charge transfer dynamics in heterostructure NiFe-LDH/N-rGO/g-C₃N₄ nanocomposite for photocatalytic pollutant removal and water splitting reactions. *Sci. Rep.* **9**(1), 2458 (2019). <https://doi.org/10.1038/s41598-019-39009-4>
41. M. Sahoo, S. Mansingh, S. Subudhi, P. Mohapatra, K. Parida, Plasmonic AuPd bimetallic nanoalloy decorated over a GO/LDH hybrid nanocomposite via a green synthesis route for robust Suzuki coupling reactions: a paradigm shift towards a sustainable future. *Catal. Sci. Technol.* **9**(17), 4678–4692 (2019). <https://doi.org/10.1039/C9CY01085H>
42. A. Behera, K. Debasmita, S. Mansingh, S. Martha, K. Parida, Facile synthesis of ZnFe₂O₄@RGO nanocomposites towards photocatalytic ciprofloxacin degradation and H₂ energy production. *J. Colloid Interface Sci.* **556**, 667–679 (2019). <https://doi.org/10.1016/j.jcis.2019.08.109>
43. L. Paramanik, K.H. Reddy, K.M. Parida, An energy band compactable B-rGO/PbTiO₃ p–n junction: a highly dynamic and durable photocatalyst for enhanced photocatalytic H₂ evolution. *Nanoscale* **11**(46), 22328–22342 (2019). <https://doi.org/10.1039/C9NR06378A>
44. S. Mansingh, D.K. Padhi, K. Parida, Bio-surfactant assisted solvothermal synthesis of Magnetic retrievable Fe₃O₄@rGO nanocomposite for photocatalytic reduction of 2-nitrophenol and degradation of TCH under visible light illumination. *Appl. Surf. Sci.* **466**, 679–690 (2019). <https://doi.org/10.1016/j.apsusc.2018.10.056>
45. K.K. Das, S. Patnaik, S. Mansingh, K. Parida, A. Behera, A. Mohanty, C. Acharya, K.M. Parida, Enhanced photocatalytic activities of polypyrrole sensitized zinc ferrite/graphitic carbon nitride n–n heterojunction towards ciprofloxacin degradation, hydrogen evolution and antibacterial studies. *J. Colloid Interface Sci.* **561**, 551–567 (2020). <https://doi.org/10.1016/j.jcis.2019.11.030>
46. K.K. Das, D.P. Sahoo, S. Mansingh, K. Parida, ZnFe₂O₄@WO₃-X/polypyrrole: an efficient ternary photocatalytic system for energy and environmental application. *ACS omega* **6**, 30401 (2021). <https://doi.org/10.1021/acsomega.1c03705>

Publisher's Note Springer Nature remains neutral with regard to jurisdictional claims in published maps and institutional affiliations.

Springer Nature or its licensor (e.g. a society or other partner) holds exclusive rights to this article under a publishing agreement with the author(s) or other rightsholder(s); author self-archiving of the accepted manuscript version of this article is solely governed by the terms of such publishing agreement and applicable law.